Performance of Photon-Number Resolving Transition-Edge Sensors With Integrated 1550 nm Resonant Cavities

D. Rosenberg, A. E. Lita, A. J. Miller, S. Nam, and R. E. Schwall

Abstract—**Many quantum-information applications require high-efficiency, low-noise, single-photon detectors that operate at visible and near-infrared wavelengths. The tunable superconducting critical temperature and anomalously low electron-phonon coupling of tungsten make it a suitable material for the fabrication of transition-edge sensors (TESs) that meet these requirements. The quantum efficiency of a typical tungsten TES detector, intrinsically around 15% at 1550 nm, can be increased by placing the tungsten detector in a resonant cavity, but the performance of a device embedded in a cavity has not been tested previously. We demonstrate that the presence of the cavity does not adversely affect the sensitivity or response time, and we report on the device characteristics of a new generation of tungsten TESs with greater than 80% quantum efficiency at 1550 nm.**

Index Terms—**Infrared detectors, photodetectors, quantum efficiency, superconducting radiation detectors.**

I. INTRODUCTION

TRANSITION-EDGE SENSORs (TESs) are microcalorimeters that provide excellent energy resolution with very low noise. A microcalorimeter consists of a thermometer and an absorber that is weakly linked to a thermal bath. When a photon is absorbed, the temperature of the system increases and then decays back to equilibrium as the heat flows to the thermal bath. TESs use the temperature dependence of the resistance at the superconducting transition as a very sensitive thermometer. The devices can be made sensitive to single photons from UV to near-infrared frequencies through the proper choice of materials and size [1]. A typical TES designed to detect near-infrared light is a small (tens of micrometers on a side), thin (tens of nanometers) square of tungsten. The absorber for a tungsten TES is the electron system, and the weak link is provided by the anomalously low electron-phonon coupling in tungsten at low temperatures.

The tungsten TES is cooled to well below the superconducting transition temperature ($T_c \sim 100$ mK) and voltage biased. The Joule heating generated by the bias causes the temperature of the electrons to be higher than the thermal bath temperature. If the voltage is adjusted so that the tungsten is in the region of superconducting transition, the system experiences negative feedback and is stable to perturbations [2]. When a photon is absorbed by the detector, the electron system of the tungsten heats up, changing its resistance, and the resulting current change is read out by a SQUID array amplifier [3], [4].

The quantum efficiency (QE) of tungsten TESs, defined as the ratio of electrical pulses out to photons incident on the detector, is typically around 15–20% broadband at 1550 nm and is limited by light being reflected from the front surface of the detector or transmitted through the tungsten. We can improve the QE by embedding the TES in a resonant cavity that maximizes the absorption in the tungsten [5]. The cavity structure discussed in this work necessitates depositing the tungsten over a metallic mirror and dielectric buffer layer and then depositing a dielectric anti-reflection coating on the tungsten. To be effective these layers must affect neither the superconducting transition temperature nor the thermal coupling of the tungsten to the bath.

II. DEVICE FABRICATION

A challenging aspect of tungsten TES fabrication is control of the superconducting critical temperature, T_c. Depositing the tungsten in situ with an underlayer of amorphous silicon and a coating of amorphous silicon (a-Si) has been found to stabilize the T_c of DC-sputtered films. Tuning of the T_c is accomplished by adjusting the sputtering pressure and power [6].

Fig. 1 shows four detectors and a schematic of the cross section, neglecting the wiring layer. The 60 nm-thick aluminum layer is deposited on a silicon substrate using electron-beam evaporation. A photoresist lift-off process is performed, leaving the squares of aluminum that will form the backside mirror of the cavity. The SiO_2 is deposited using plasma-enhanced chemical vapor deposition, and the a-Si/W/a-Si trilayer is DC-sputtered. The next two steps, patterning the tungsten into squares and depositing the wiring layer, are outlined in Fig. 2. The trilayer is patterned with photoresist and the top layer of a-Si is ion milled to expose the tungsten, which is etched with a commercial tungsten etch. The wafer is again coated with photoresist and patterned, exposing the edges of the trilayer squares for the wiring layer. The a-Si is ion-milled to expose the tungsten, and the 60 nm of aluminum for the wiring layer is e-beam evaporated directly onto the tungsten. The final step is the deposition of the anti-reflective layer. The photoresist is removed and another 50 nm of amorphous silicon is sputtered to complete the cavity structure.

The authors are with the National Institute of Standards of Technology, Boulder, CO 80305 USA (e-mail: rdanna@boulder.nist.gov).
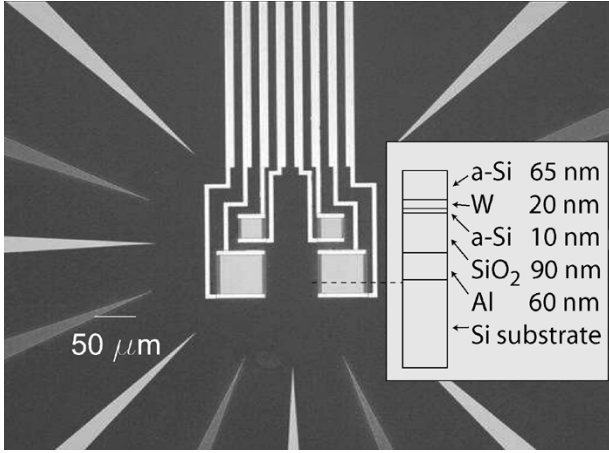
Fig. 1. The center of the figure contains four detectors with sides of 25 μm (upper) and 50 μm (lower). The parallel lines at the top of the figure are the aluminum leads used to make electrical contact to the detector. The tapered lines pointing to the center are an aid for alignment to the optical fiber.
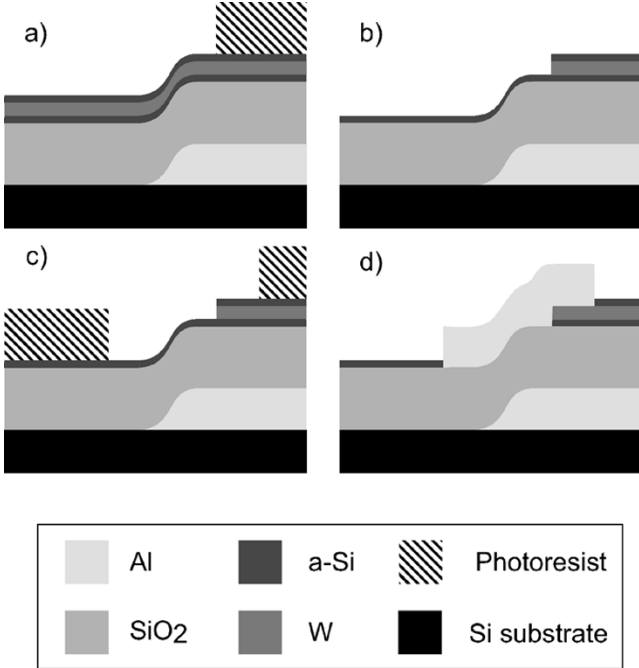

Fig. 2. Fabrication steps for patterning the tungsten and depositing the aluminum wiring layer. (a) Photoresist is applied and patterned for the tungsten etch. (b) The top layer of amorphous silicon is ion milled and the tungsten is etched, resulting in squares of tungsten lying over the aluminum mirrors. (c) Photoresist is reapplied and patterned for the wiring layer. (d) The top layer of amorphous silicon is ion milled and aluminum is e-beam evaporated. The thickness of the photoresist layers and the width of the aluminum wiring layers are not to scale.

III. DEVICE PERFORMANCE

A. Superconducting Critical Temperature

As discussed above, the tungsten is sandwiched between two layers of amorphous silicon to yield reproducible critical temperatures. Improvement of the process reliability allows us to control the T_c of our devices. A low T_c is desirable to reduce the heat capacity of the device, making it more sensitive, but a high T_c results in a faster device. The devices we describe in this
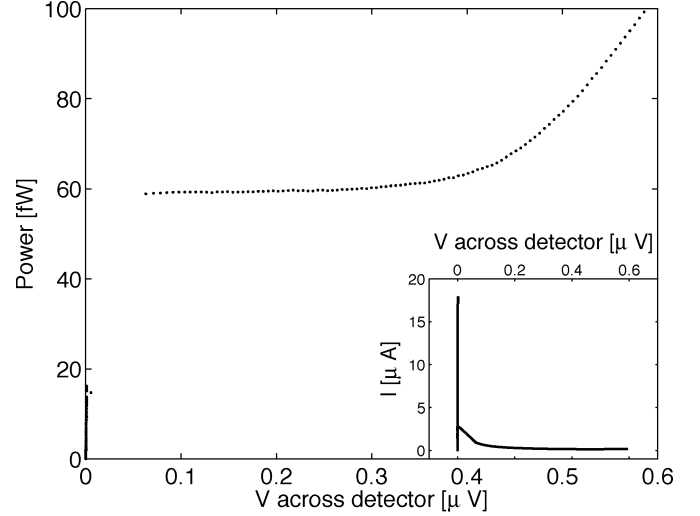

Fig. 3. Power and current as a function of voltage for 25 μm × 25 μm sensor. Below 0.4 μV the sensor is self-biased and the power is approximately constant as a function of voltage. The power in the self-biased region can be used to estimate the electron-phonon coupling.

paper had transition temperatures of 110 ± 5 mK. This allowed us to cool the samples in an adiabatic demagnetization refrigerator [7] while still providing the sensitivity to detect single photons at near-infrared wavelengths.

B. I-V Characteristics

The inset to Fig. 3 displays the I-V curve for a 25 μm sensor embedded in a resonant cavity designed to maximize absorption at 1550 nm. The main part of the figure shows the power dissipated in the sensor as a function of the voltage across the sensor. The power in the self-biased region (where the power as a function of voltage is relatively constant), is known as the quiescent power and is given by

$$P = V\kappa\left(T^n - T_c^n\right), \qquad (1)$$

where V is the sensor volume, κ is the electron-phonon coupling constant, and n is around 5 for electron-phonon coupling below 1 K. We can extract κ by fitting to (1) the variation of P_0 with temperature close to T_c. Although we have not measured P_0 as a function of temperature for the devices described in this paper, we have done so for other tungsten devices deposited under similar conditions. We obtained $\kappa \approx 0.3\,\mathrm{nW}/(\mathrm{K}^5 \cdot \mu\mathrm{m}^3)$ for devices with $T_c = 74$ mK, about an order of magnitude lower than typical values of κ for other metals $(2-3\,\mathrm{nW}/(\mathrm{K}^5 \cdot \mu\mathrm{m}^3))$ [8], [9].

At temperatures well below T_c, the thermal conductance $g = dP/dT \sim nP_0/T_c$. The data give $P_0 \approx 60$ fW for the 25 μm device and $P_0 \approx 400$ fW for the 50 μm device. If the sharpness of the superconducting transition is the same for both devices, the quiescent power should be proportional to the sensor volume. A possible explanation for the discrepancy is the presence of an additional heat load of 53 fW. We have seen prior evidence of a heat leak of this order, which could be due to RF power coupling to the sensor through the leads. Assuming a heat load of 53 fW, the thermal conductances for the 25 μm and 50 μm devices are 5.14 μW/K and 20.6 μW/K, respectively.
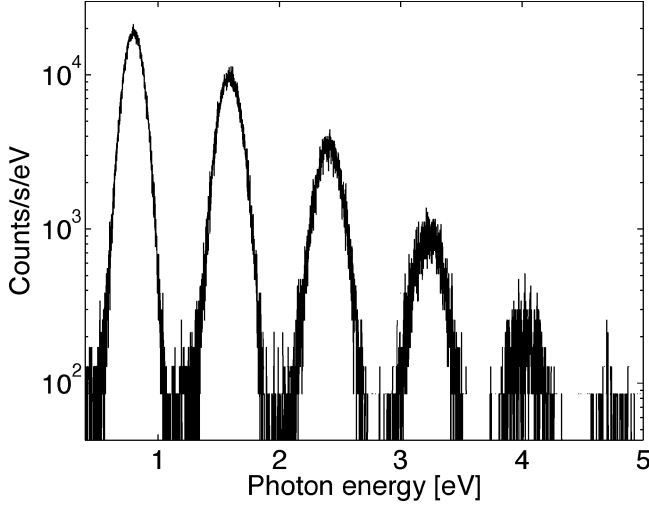
Fig. 4. Histogram of pulse heights for a 25 μm sensor embedded in a cavity and illuminated with a pulsed source of 1550 nm photons. The FWHM for this device is 0.20 eV, giving excellent discrimination between one- and two-photon events.

We will use these numbers in the next section to calculate the intrinsic time constant of the device.

C. Pulse Decay Time

The intrinsic time constant of the system is $\tau_0 = C/g$, where C is the heat capacity. For this calculation, we will use the heat capacity for normal tungsten multiplied by the expected BCS increase in heat capacity just below T_c. The electronic heat capacity for normal W is $C = \gamma T$, where $\gamma = 1.3 \, \text{mJ/mole} - \text{K}^2$ [10]. For our 25 μm $\times$ 25 μm $\times$ 20 nm and 50 μm $\times$ 50 μm $\times$ 20 nm sensors and critical temperature, we obtain $C_{25 \, \mu\text{m}} = 0.45$ fJ/K and $C_{50 \, \mu\text{m}} = 1.8$ fJ/K. Using these numbers and the thermal conductances we calculated in Section III-B, we find that $\tau_0 \approx 87 \, \mu$s for both devices.

The actual time constant of the device is shorter due to electrothermal feedback and is given by

$$\tau_{\text{ETF}} = \frac{\tau_0}{\left(1 + \frac{\alpha}{n}\right)}, \qquad (2)$$

where $\alpha = (d \ln R/d \ln T)_{V=\text{const}}$ describes the sharpness of the superconducting transition [2]. We can use the measured value of τ_{ETF} and the intrinsic time constant to estimate α. The time constants of both devices were approximately 5 μs, giving $\alpha \approx 83$. We have also measured time constants as long as 20 μs for identically fabricated sensors from the same wafer. Because the decay time of the pulses depends on α, the sharpness of the superconducting transition, it is likely that the differences in decay times are due to differences in α.

D. Noise and Resolution

Fig. 4 shows a histogram of pulse height for illumination of a 25 μm detector with a pulsed 1550 nm source. Our measured values for the full width half maximum (FWHM) of the small and large devices are respectively 0.20 eV and 0.28 eV.

The theoretical energy resolution limit is [2]

$$\Delta E_{\text{FWHM},\alpha} = 2.36 \sqrt{4kT_c^2 C \left(\frac{1}{\alpha}\right) \sqrt{\frac{n}{2}}}. \qquad (3)$$

In Section III-C we estimated that $\alpha \approx 83$, giving expected resolutions of $\Delta E_{\text{FWHM},25 \, \mu\text{m}} \approx 0.035$ eV and $\Delta E_{\text{FWHM},50 \, \mu\text{m}} \approx 0.07$ eV. However, as pointed out in [11], the expected FWHM will be larger because not all of the energy of each absorbed photon is captured in the tungsten electron system. Typically only about 40% of the energy is captured [11], resulting in expected energy resolutions of 0.088 eV and 0.18 eV.

We can also estimate α from the saturation energy above which additional photons do not change the temperature of the electrons. The measured saturation energies for the small and large devices are 6.4 eV and 21.6 eV. The saturation energy $E_{max} \approx CT_c/f\alpha$ [11], where f is the fraction of energy absorbed in the electron system. Again using $f = 0.4$, we find that $\alpha_{25 \, \mu\text{m}} \approx 121$ and $\alpha_{50 \, \mu\text{m}} \approx 143$, giving $E_{\text{FWHM},25 \, \mu\text{m}} \approx 0.073$ eV and $\Delta E_{\text{FWHM},50 \, \mu\text{m}} \approx 0.13$ eV.

The ΔE_{FWHM} we measure, while on the same order as what we calculated above, is consistently larger than that obtained in calculations. We expect our energy resolution to be worse than that given by (3) because we do not perform the optimal filtering assumed in the derivation. We have not yet determined whether the discrepancy between the calculated and measured resolution is due to noise from our electronics, nonoptimal filtering, or excess noise in the sensors. However, excess noise in TESs has been observed by several groups [12], [13], and recent work suggests that the noise can be reduced by applying magnetic fields to the sensors or by changing their geometry [14]. By reducing the excess noise and improving the fraction of energy collected, we could obtain performance similar to that shown in Fig. 4 at higher temperatures and speeds.

E. Efficiency

Details on the components forming the optical cavity can be found elsewhere [5]. Measurements and simulations of the layers indicate that 85% to 90% of the incident 1550 nm photons should be absorbed in the tungsten substrate. Careful measurements [15] indicate that the quantum efficiency (QE) of the detector, measured from the top of the cryostat, is $82 \pm 2\%$. We believe that the discrepancy is due to system losses arising from bends in the optical fiber carrying the light and misalignment of the fiber to the detector. We are working to reduce our system losses to enable the end-to-end system efficiency to approach the intrinsic QE of the device.

IV. CONCLUSION

With their low noise and photon-counting ability, transition-edge sensors are the enabling technology for a number of quantum-information experiments [16], [17]. They become even more valuable if their quantum efficiency is increased by placing them inside a resonant cavity. We have shown that the addition of a cavity structure around the sensor does not degrade the performance of the detector and improves the optical performance. Our new generation of tungsten TESs

have quantum efficiency greater than 80% but still maintain their excellent number resolving ability at 1550 nm.

REFERENCES

[1] A. J. Miller, B. Cabrera, R. M. Clarke, E. Figueroa-Feliciano, S. Nam, and R. W. Romani, *IEEE Trans. Appl. Supercond.*, vol. 9, p. 4205, 1999.

[2] K. D. Irwin, *Appl. Phys. Lett.*, vol. 66, p. 1998, 1995.

[3] R. P. Welty and J. M. Martinis, *IEEE Trans. Magn.*, vol. 27, p. 2924, 1991.

[4] M. E. Huber *et al.*, *IEEE Trans. Appl. Supercond.*, vol. 11, p. 1251, 2001.

[5] D. Rosenberg, S. Nam, A. J. Miller, A. Salminen, E. Grossman, R. E. Schwall, and J. M. Martinis, *Nucl. Instrum. Meth. Phys. Res. Sect. A*, vol. 520, p. 537, 2004.

[6] A. E. Lita *et al.*, *Trans. Appl. Supercond.*, vol. 15, no. 2, Jun 2005.

[7] D. A. Wollman, K. D. Irwin, G. C. Hilton, L. L. Dulcie, D. E. Newbury, and J. M. Martinis, *J. Microscopy*, vol. 188, p. 196, 1997.

[8] M. L. Roukes, M. R. Freeman, R. S. Germain, R. C. Richardson, and M. B. Ketchen, *Phys. Rev. Lett.*, vol. 55, p. 422, 1985.

[9] F. C. Wellstood, C. Urbina, and J. Clarke, *Appl. Phys. Lett.*, vol. 49, p. 5942, 1994.

[10] C. Kittel, *Introduction to Solid State Physics*.   New York: Wiley, 1986.

[11] B. Cabrera, R. M. Clarke, P. Colling, A. J. Miller, S. Nam, and R. W. Romani, *Appl. Phys. Lett.*, vol. 73, p. 735, 1998.

[12] A. Luukanen, K. M. Kinnunen, A. K. Nuottajarvi, H. F. C. Hoevers, W. M. B. Tiest, and J. P. Pekola, *Phys. Rev. Lett.*, vol. 90, p. 238 306, 2003.

[13] Y. Takei *et al.*, *Nucl. Instrum. Meth. Phys. Res. Sect. A*, vol. 523, p. 134, 2004.

[14] J. N. Ullom *et al.*, *Appl. Phys. Lett.*, vol. 84, p. 4206, 2004.

[15] D. Rosenberg *et al.*, unpublished.

[16] G. Di Giuseppe *et al.*, *Phys. Rev. A*, vol. 68, p. 063 817, 2003.

[17] E. Knill, R. Laflamme, and G. J. Milburn, *Nature*, vol. 409, p. 46, 2001.